https://doi.org/10.5194/egusphere-2026-3682
Preprint. Discussion started: 12 August 2026

Mechanistic Insights into Nitric Sulfuric Acid Formation and Its Enhancement of Sulfuric Acid-Ammonia Nucleation under Severe Urban Pollution

Chengyan Zhang[‡1], Guanhua Wang[‡1], Xiaokai Guo[1], Yaogeng Li[1], Xueping Feng[1], Yuan Zuo[2], Rui Wang[*1]

[1] *Shaanxi Key Laboratory of Catalysis, School of Chemical & Environment Science, Shaanxi University of Technology, Hanzhong, Shaanxi 723001, P. R. China*

[2] *Yulin Environmental Protection Engineering Co., Ltd., Yulin, Shaanxi 719000, P. R. China.*

Abstract

Organosulfates (OSs) constitute an important component of secondary organic aerosols (SOA). Although previous studies have investigated the aerosol nucleation of OSs such as glycolic acid sulfate and methyl hydrogen sulfate, exploring the aerosol nucleation behavior of additional OSs remains essential. Herein, the formation mechanism of nitric sulfuric acid (NSA) from the reaction of sulfur trioxide (SO_3) with nitric acid (NA)and its role in sulfuric acid (SA)-ammonia (A) aerosol nucleation was investigated using quantum chemical calculations combined with kinetic simulations. Our results demonstrate that NSA can be formed rapidly and stably in the gas phase with a low barrier of 3.61 kcal·mol^{-1}. The SO_3 + HNO_3 reaction remains competitive with major atmospheric SO_3 loss pathways, including reactions of SO_3 + HCOOH, SO_3 + C_6H_5COOH and NH_3-catalyzed reactions, and even H_2O-catalyzed hydrolysis under dry conditions. Kinetic simulations further demonstrate that NSA significantly accelerates SA-A nucleation, with rates reaching ~ 10^{-3} cm^{-3} s^{-1} under heavily polluted urban conditions (e.g., Beijing), corresponding to a five-order-of-magnitude enhancement over binary clusters and a 10^{1}-10^{11}-fold increase relative to nitric acid. These findings underscore the importance of incorporating NSA into atmospheric aerosol models.

* Corresponding authors. Tel: +86-0916-2641083, Fax: +86-0916-2641083.

E-mail: wangrui830413@163.com (R. Wang)

‡ Chengyan Zhang and Guanhua Wang contributed equally to this work.

https://doi.org/10.5194/egusphere-2026-3682
Preprint. Discussion started: 12 August 2026

1 Introduction

Atmospheric aerosols exert profound effects on both public health and the global climate (Sun et al., 2025; McNeill, 2017; Chu et al., 2019; Lee et al., 2019)). Inhalation of fine particulate matter has been linked to elevated risks of cardiorespiratory diseases (Pöschl, 2005;Brook et al., 2010; Pope et al., 2018;), broader systemic disorders (Zhao et al., 2025), and premature death. Within the climate system, aerosols influence radiative forcing directly by modifying the interaction between atmospheric particles and incoming radiation (Haywood and Boucher, 2000) and indirectly by acting as cloud condensation nuclei (CCN) (Duan et al., 2018; Casans et al., 2025; Silva et al., 2025; Williamson et al., 2019), which influence cloud optical properties and persistence. New particle formation (NPF) (Lee et al., 2019; Kulmala et al., 2013; Zhang et al., 2012) constitutes an important pathway for atmospheric aerosol production, beginning with the formation of molecular clusters from gaseous precursors and progressing toward particles large enough to exert climatic effects. However, the inherent complexity of NPF presents a central challenge, as its core mechanisms resist full elucidation through either field observations (Mäkelä et al., 1997) or laboratory studies (Chen et al., 2017; Kürten et al., 2014) alone. Thus, a molecular-level (Zhang et al., 2022; Wang et al., 2017) understanding of the processes governing NPF (Lee et al., 2019; Kulmala et al., 2013) is essential to accurately predict aerosol impacts and to formulate effective haze mitigation policies.

Sulfuric acid (SA) is well established as a critical precursor in NPF (Sipilä et al., 2010). In the lower atmosphere, its nucleation is enhanced by ammonia (A) (Almeida et al., 2013; Yu et al., 2018), the dominant alkaline gas, promotes nucleation by stabilizing acid-base cluster formation. Nevertheless, nucleation rates predicted from the binary SA-A system (Kirkby et al., 2011) are consistently and significantly lower than those observed in the ambient atmosphere. This systematic underestimation implies the involvement of additional stabilizing species in the nucleation clusters. In recent years, considerable research has focused on ternary systems incorporating organic amines (Zuo et al., 2021; Xu et al., 2020), other acids (Li et al., 2024a; Li et al., 2024b), and highly oxidized organic compounds (Berndt et al., 2016; Dam et al., 2023), which have successfully explained NPF events in certain environments. Yet, the exceptionally high nucleation rates characteristic of many SA-dominated environments continues to challenge current mechanistic understanding, suggesting that critical aspects of the nucleation process remain unresolved.

https://doi.org/10.5194/egusphere-2026-3682
Preprint. Discussion started: 12 August 2026

Beyond conventional precursors, recent studies have highlighted the importance of novel species generated from the reactions of SO_3 with trace species in driving NPF (Yang et al., 2021; Liu et al., 2019). For instance, Liu et al. (Liu et al., 2019) demonstrated that methanol reacts with SO_3 to form methyl hydrogen sulfate (MHS), which markedly enhances SA-dimethylamine (DMA) nucleation under the dry, polluted, and CH_3OH-rich conditions typical of northern China in winter. Similarly, Zhang et al (Zhang et al., 2024) demonstrated that glycolic acid sulfate (GAS), generated through the interaction of glycolic acid with SO_3, vigorously promotes SA-DMA nucleation. This enhancement is particularly low SA concentrations, where the nucleation rate can be amplified up to 800 at 278 K. Another relevant product is nitric sulfuric acid (NSA), formed via the $SO_3 + HNO_3$ reaction (Long et al., 2022). The molecular structure of NSA, featuring both -OH and $-SO_3H$ functional groups, enables it to act as a versatile bridge, forming multiple hydrogen bonds with nucleation precursors. This distinctive structural characteristic motivates a systematic investigation into the role of NSA in NPF.

In this work, we comprehensively examine the nucleation mechanism of the $(SA)_x(A)_y(NSA)_z$ ($y \le x + z \le 3$) system using a combined approach of density functional theory (DFT) calculations and the atmospheric clusters dynamic code (ACDC). To clarify the distinct roles of inorganic acids and sulfates in enhancing SA-A nucleation, we performed a comparative analysis of the NSA-SA-A and NA-SA-A systems. This study aims to (*i*) quantify the enhancement of SA-A-driven NPF rates by NSA and (*ii*) clarify the influence of NSA on the evolution pathways of these clusters.

2 Computational details

2.1 Electronic structure calculations. The molecular clusters of $(SA)_x(A)_y(NSA)_z$ ($y \le x + z \le 3$) were examined using quantum chemical calculations coupled with a multi-step global minimum search. Specifically, initial structures were stochastically generated using the ABCluster program (Zhang and Dolg, 2015, 2016) producing $n \times 1000$ ($1 < n \le 4$) candidates for each system. These structures were first pre-optimized at the PM6 semi-empirical level (Stewart, 2013; Partanen et al., 2016). Given the reliable performance of the M06-2X functional for noncovalent interactions and atmospheric cluster systems, the 100 lowest-energy configurations from the $n \times 1000$ ($1 < n \le 3$) were selected for further optimization at the M06-

https://doi.org/10.5194/egusphere-2026-3682
Preprint. Discussion started: 12 August 2026

2X/6-31G(*d*,*p*) level (Elm et al., 2012). Subsequently, the 10 most stable structures were refined at the M06-2X/6-311++G(2*df*,2*pd*) level (Elm and Mikkelsen, 2014), and the global minimum was identified based on Gibbs free energy. Finally, high-accuracy single-point energy for the gas-phase and aerosol structures were subsequently evaluated using ORCA 4.2.0 (Neese, 2018) at the CCSD(T)-F12/cc-pVDZ-F12 and DLPNO-CCSD(T)/aug-cc-pVDZ computational levels, respectively.

In addition, the proton transfer parameter ρ_{PT} (Hunt et al., 2003; Wang et al., 2021; Liu et al., 2018) was used to quantify proton transfer in hydrogen bonds. This parameter was calculated from interatomic distances and applied to assess the degree of ionization in the clusters, considering both the contraction of hydrogen bonds (HB) and the elongation of covalent HB bonds. The expression for ρ_{PT} is given below:

$$\rho_{PT} = (r_{OH} - r_{OH}^{\theta}) - (r_{H\cdots N} - r_{H\cdots N}^{\theta}) \quad (1)$$

Here, r_{OH} and r_{OH}^{θ} denote the O-H lengths in NSA or SA and in the corresponding isolated monomer, respectively. Likewise, $r_{H\cdots N}$ and $r_{H\cdots N}^{\theta}$ denote the HB distances within the NSA-A and SA-A clusters and the H-N bond length in fully protonated A. In HB clusters, the initial term approaches zero, resulting in a negative value of ρ_{PT}. When complete proton transfer to A occurs, the second term vanishes and ρ_{PT} becomes positive. A ρ_{PT} value close to zero indicates an approximately symmetric sharing of the proton between the acid and base (Hunt et al., 2003; Wang et al., 2021; Liu et al., 2018).

2.2 ACDC simulations. The Atmospheric Cluster Dynamics Code (ACDC) model (McGrath et al., 2012) was applied to describe the temporal evolution of nucleation rates, steady-state cluster populations, and cluster growth pathways within the SA-A-NSA system. Thermodynamic data obtained from the M06-2X/6-311++G(2*df*,2*pd*) (Elm and Mikkelsen, 2014; Holtomo et al., 2021) calculations served as input parameters for the simulations. The birth-death equations, governing the temporal evolution of cluster concentrations, were numerically integrated using by the ode15s solver in the MATLAB-R2013a program (Shampine and Reichelt, 1997). The general form of the birth-death equations is given by Eq. (2).

$$\frac{dc_i}{dt} = \frac{1}{2}\sum_{j<i}\beta_{j,(i-j)}C_jC_{(i-j)} + \sum_j \gamma_{(i+j)\to i}C_{i+j} - \sum_j \beta_{i,j}C_iC_j - \frac{1}{2}\sum_{j<i}\gamma_{i\to j}C_i + Q_i - S_i \quad (2)$$

https://doi.org/10.5194/egusphere-2026-3682
Preprint. Discussion started: 12 August 2026

Here, c_i denotes the concentration of cluster i, $\beta_{i,j}$ is the collision coefficient between clusters i and j, and $\gamma_{(i+j)\rightarrow i}$ signifies the evaporation coefficient for the dissociation of $i + j$ into i and j. The term Q_i accounts for any extra source for cluster i, while the sink term S_i reflects the losses associated with cluster i. [SA] fluctuated between 10^4 to 10^8 molecules·cm^{-3} (Rong et al., 2020; Almeida et al., 2013; Kuang et al., 2008), while [A] ranged from 10^7 to 10^{11} molecules·cm^{-3} (Liu et al., 2021) and the corresponding [NSA] was between 10^3 and 10^7 molecules·cm^{-3}. An external loss rate, represented by a coagulation sink value of 2×10^{-2} s^{-1} (Yao et al., 2018) was adopted, corresponding to the median value observed in polluted regions. A more detailed description of the collision and evaporation rates will be provided in the corresponding section, specifically in Part S2 of the Supplementary Information.

3 Results and discussion

3.1 Gas-phase formation of NSA and its atmospheric concentration

Fig. 1 presents the intrinsic reaction coordinate pathway for the reaction between SO_3 and HNO_3, accompanied by interaction region indicator (IRI) analysis to elucidate the evolution of atomic interaction strengths along the reaction pathway. Fig. 1 illustrates that the reaction follows a mechanism consisting of two successive steps. At the first stage of the reaction, the appearance of a blue region on the IRI isosurface between SO_3 and HNO_3 indicates the formation of a weakly bound $SO_3\cdots HNO_3$ reactant complex (a). This complex adopts a six-membered ring configuration, exhibiting a stabilization energy of 6.70 kcal·mol^{-1}, in close agreement with the previously reported value of 6.94 kcal·mol^{-1} (Long et al., 2022). As the system evolves along the reaction coordinate, the blue region on the isosurface becomes more pronounced, reflecting a gradual strengthening of the attractive interaction. Subsequently, the reaction crosses transition state (c) with an associated energy barrier of 3.61 kcal·mol^{-1}, comparable to the value of 3.75 kcal·mol^{-1} reported by Long et al (Long et al., 2022). Concurrently, the original O4-H bond progressively weakens, while a new bond forms between the O6 atom of HNO_3 and the S atom of SO_3. At the final stage of the reaction, the IRI isosurface is dominated by a large green region, indicating the generation of a stable nitric sulfuric acid (O_2NOSO_3H, NSA) characterized by typical covalent bond features.

To evaluate the relative significance of the SO_3 + HNO_3 reaction under a wide range of atmospheric conditions, rate ratios were calculated for the SO_3 + HNO_3 reactions relative to the

https://doi.org/10.5194/egusphere-2026-3682
Preprint. Discussion started: 12 August 2026

reactions of SO_3 + HCOOH (Eq. 3), SO_3 + C_6H_5COOH (Eq. 4), NH_3-catalyzed SO_3 + NH_3 (Eq. 5) and H_2O-catalyzed hydrolysis of SO_3 (Eq. 6). The calculations considered H_2O at 20%-80% relative humidity (RH), HNO_3 at 10^9-10^{12} molecules·cm^{-3}, HCOOH at 10^9-10^{12} molecules·cm^{-3}, C_6H_5COOH at 10^6-10^{10} molecules·cm^{-3} and NH_3 at 10^{10}-10^{13} molecules·cm^{-3}.

$$\frac{v_{R1}}{v_{R2}} = \frac{k_{R1}[SO_3][HNO_3]}{k_{R2}[SO_3][HCOOH]} = \frac{k_{R1}[HNO_3]}{k_{R2}[HCOOH]} \quad (3)$$

$$\frac{v_{R1}}{v_{R3}} = \frac{k_{R1}[SO_3][HNO_3]}{k_{R3}[SO_3][C_6H_5COOH]} = \frac{k_{R1}[HNO_3]}{k_{R3}[C_6H_5COOH]} \quad (4)$$

$$\frac{v_{R1}}{v_{R4}} = \frac{k_{R1}[SO_3][HNO_3]}{k_{R4}[SO_3\cdots NH_3][NH_3]} \quad (5)$$

$$\frac{v_{R1}}{v_{R5}} = \frac{k_{R1}[SO_3][HNO_3]}{k_{R5}[SO_3\cdots H_2O][H_2O]} \quad (6)$$

Here, k_{R1}, k_{R2}, k_{R3}, k_{R4}, and k_{R5} denote the rate coefficients for the reactions of SO_3 + HNO_3, SO_3 + HCOOH, SO_3 + C_6H_5COOH and NH_3-catalyzed SO_3 + NH_3, H_2O-catalyzed hydrolysis of SO_3, respectively (Table S2), while [HNO_3] (Long et al., 2022), [H_2O] (Wang et al., 2025), [HCOOH] (Hazra and Sinha, 2011), [C_6H_5COOH] (Smith et al., 2020) and [NH_3] (Li et al., 2018) represent the corresponding reactant concentrations.

As shown in Fig. 2, the SO_3 + HNO_3 reaction remains more efficient than the SO_3 + HCOOH reaction even under conditions of low HNO_3 (< 10^9 molecules·cm^{-3}) and high HCOOH (> 10^{12} molecules·cm^{-3}) concentrations, with a rate ratio (v_{R1}/v_{R2}) approaching 50. Under elevated HNO_3 concentrations (10^{10}-10^{12} molecules·cm^{-3}) and relatively low C_6H_5COOH (10^7-10^8 molecules·cm^{-3}) and NH_3 (10^{10}-10^{11} molecules·cm^{-3}) concentrations, the SO_3 + HNO_3 reaction can effectively compete with both the SO_3 + C_6H_5COOH and NH_3-catalyzed SO_3 + NH_3 reactions, with v_{R1}/v_{R3} and v_{R1}/v_{R4} reaching values of up to 10^1-10^3. More importantly, when the HNO_3 concentration exceeds 10^{12} molecules·cm^{-3} under dry conditions (RH = 20%), the SO_3 + HNO_3 reaction becomes competitive with the H_2O-catalyzed hydrolysis of SO_3, yielding v_{R1}/v_{R5} values of 1-3. Taken together, these results demonstrate that the SO_3 + HNO_3 reaction can compete with several major atmospheric SO_3 loss pathways over a wide range of atmospherically relevant conditions. Therefore, the reaction between SO_3 and HNO_3 may represent an important atmospheric sink of SO_3, particularly in polluted urban and industrial environments with elevated HNO_3 levels, where it may substantially

https://doi.org/10.5194/egusphere-2026-3682
Preprint. Discussion started: 12 August 2026

influence the atmospheric fate of SO_3 and associated sulfur chemistry.

In the absence of atmospheric field measurements for gas-phase NSA, thermodynamic equilibrium calculations were applied to estimate its atmospheric concentration and to assess its potential impact on NPF. The concentration of its key precursor, SO_3, exhibits pronounced regional variability. SO_3 concentrations in regions such as Beijing, are around 10^6 molecules·cm^{-3} (Yao et al., 2020), while substantially higher levels, are observed in in industrial emission zones. Atmospheric NA concentration can similarly approach 10^{12} molecules·cm^{-3}. By combining the plausible concentration ranges of both precursors within the anthropogenically influenced troposphere (258.15-298.15 K), the atmospheric concentration of NSA is estimated to range from 10^3 to 10^7 molecules·cm^{-3}. The detailed calculation of the calculation procedure can be found in Part S1 of the Supplement.

3.2 The vital role of NSA in SA-A nucleation: impacts of urban pollutants

Here, a systematic conformational analysis was initially conducted to examine the influence of NSA on intermolecular interactions within NSA-SA-A clusters. The stability of the resulting clusters was subsequently assessed through thermodynamic analysis. Furthermore, to provide deeper insight into the nucleation mechanisms and the enhancement strength of NSA, a series of ACDC simulations was conducted under a range of representative atmospheric conditions.

3.2.1 Geometrical structure analysis

Electrostatic potential (ESP) mapped on the molecular van der Waals (vdW) surface was first employed to identify potential active binding sites (Fig. S6). Owing to its dual hydrogen-bond donor and acceptor capabilities, NSA readily forms stable clusters with SA and A via hydrogen-bonding interactions. To further quantify these interactions, reduced density gradient (RDG) analysis was performed (Fig. S7). Compared with the binary SA·A cluster, NSA-containing clusters exhibit progressively enhanced intermolecular interactions, as indicated by the emergence of additional blue spikes in the SA·A·NSA cluster and a further leftward shift of the blue spike upon successive NSA incorporation. These findings indicate that NSA strengthens noncovalent interactions and promotes cluster stabilization. Building on these interaction characteristics, Fig. 3 presents the lowest-energy structures of the ternary NSA-SA-A clusters identified from the potential energy surface. Notably, these global minimums provide structural support for the interaction analysis discussed above. With increasing cluster size, the molecular architecture generally evolves from

https://doi.org/10.5194/egusphere-2026-3682
Preprint. Discussion started: 12 August 2026

ring-like to cage-like configurations. Within these lowest-energy clusters, NSA molecules are incorporated into the SA-A framework primarily through HBs (blue dashed lines) and proton transfer interactions. Both SA and NSA can act as proton donors to A, leading to the formation of stabilized ion pairs, including $[HSO_4]^-[NH_4]^+$ and $[NSA]^-[NH_4]^+$.

To further elucidate the proton-transfer behavior, the proton transfer parameter (ρ_{PT}) was calculated for each cluster. As listed in Table 1, all investigated NSA-SA-A clusters exhibit positive ρ_{PT} values, confirming that proton transfer takes place in every case. In general, the number of protons transferred is consistent with the number of A molecules present in the cluster. While SA remains the preferred proton donor, NSA also participates in proton donation upon incorporation of additional A molecules. These molecular-level results highlight the crucial role of NSA in stabilizing the ternary SA-A clusters. Overall, NSA functions analogously to SA as an effective proton donor, thereby contributing to the stabilization of the most energetically favorable cluster configurations.

To further elucidate nucleation processes relevant to atmospheric aerosol formation, the Gibbs free energy of formation (ΔG) a key thermodynamic descriptor governing nucleation propensity, was calculated. Fig. 4 presents the ΔG values (kcal·mol^{-1}) at 278.15 K for $(SA)_x(A)_y(NSA)_z$ ($y \leq x + z \leq 3$) clusters. For clusters containing the same total number of acid and base molecules, ΔG decreases systematically with increasing numbers of NSA molecules, indicating NSA incorporation progressively enhances thermodynamic stability. Furthermore, at a fixed number of base molecules, ΔG decreases with increasing acid abundance, further reinforcing the stabilizing role of acid-base interactions. Importantly, the stability trend observed at 278.15 K is consistent across other atmospherically relevant temperatures (258.15 K, 268.15 K, 288.15 K and 298.15 K; Table S3), where lower temperatures generally favor stronger stabilization of cluster structures. These thermodynamic results are fully consistent with the structural and interaction analyses discussed above, collectively confirming that NSA plays a significant role in enhancing the stability of multicomponent acid-base clusters under atmospheric conditions.

3.2.2 Cluster formation rates

Fig. 5 illustrates the effects of temperature (T) and precursor concentration on the formation rates (J) of SA-A-NSA clusters under atmospherically relevant conditions. As shown in Fig. 5(a), the J exhibits a pronounced dependence on T over the range of 258.15-298.15 K. Specifically, under all investigated [NSA] conditions, J increases significantly with decreasing T, showing an

https://doi.org/10.5194/egusphere-2026-3682
Preprint. Discussion started: 12 August 2026

enhancement of up to 10-15 orders of magnitude, which is primarily attributed to the reduced cluster evaporation rate at lower *T*. In addition to *T*, the concentration of NSA plays a decisive role in governing cluster formation. At 278.15 K, increasing [NSA] from 10^3 to 10^7 molecules·cm^{-3} leads to an increase in *J* from 10^{-11} to 10^0 cm^{-3} s^{-1}, indicating a clear positive correlation between NSA abundance and nucleation rates. These results highlight that lower *T* and elevated [NSA] jointly promote SA-A-NSA cluster formation.

Fig. 5(b) further presents the dependence of *J* on [A] under different [SA] at *T* = 278.15 K and [NSA] = 10^6 molecules·cm^{-3}. As [A] increases from 10^7 to 10^{11} molecules·cm^{-3}, *J* increases continuously across all cases. For example, at [SA] = 10^8 molecules·cm^{-3}, *J* increases 10^{-6} to 10^3 cm^{-3} s^{-1}, indicating that A, as a base, can effectively stabilize clusters via acid-base interactions and thus plays a crucial role in the nucleation process. However, the enhancement is not strictly linear: at lower [A] (10^7 molecules·cm^{-3}), *J* increases by approximately six orders of magnitude, whereas at higher [A] (10^{11} molecules·cm^{-3}), the increase is reduced to about four orders of magnitude, suggesting a gradual saturation of the promoting effect. Overall, these results demonstrate that increasing both [A] and [SA] significantly enhances cluster formation, consistent with the strengthened intermolecular interactions and improved stability discussed above.

3.2.3 The nucleation mechanism

To elucidate the role of NSA in cluster formation, the primary growth pathways were further analyzed at 278.15 K under representative atmospheric concentrations ([SA] = 10^6 molecules·cm^{-3}, [NSA] = 10^6 molecules·cm^{-3}, [A] = 10^9 molecules·cm^{-3}; Fig. 6 (a)). Two distinct growth routes were identified: one is governed primarily by SA-A interactions (black arrows), corresponding to the classical binary nucleation mechanism reported previously. In contrast, the second pathway involves NSA participation (orange arrows), indicating an alternative NSA-mediated growth channel. In the NSA-involved pathway, cluster growth is initiated by the formation of an $(A)_1$·$(NSA)_1$ dimer, which subsequently grows via collisions with additional NSA molecules or other $(A)_1$·$(NSA)_1$ cluster. These intermediates further evolve via successive condensation with SA, A, NSA or additional $(A)_1$·$(NSA)_1$ cluster, ultimately approaching larger stable assemblies beyond the size limit of the present simulations. This distinct growth behavior demonstrates that NSA is not merely a spectator species but actively participates in and facilitates cluster growth, thereby providing an additional pathway for atmospheric nucleation.

https://doi.org/10.5194/egusphere-2026-3682
Preprint. Discussion started: 12 August 2026

The relative contributions of NSA-involved and non-NSA pathways to cluster growth are quantitatively evaluated using the flux-out branching ratio under different conditions. As shown in Fig. 6(b), at 278.15 K with [SA] = 10^6 molecules·cm^{-3} and [A] = 10^9 molecules·cm^{-3}, the nucleation mechanism exhibits a strong dependence on [NSA]. At low NSA concentrations (10^3-10^4 molecules·cm^{-3}), representative of conditions such as southern Ontario, Canada (Zbieranowski and Aherne, 2012), cluster growth proceeds almost exclusively via the non-NSA pathway. As [NSA] increases to 10^5 molecules·cm^{-3} (e.g., Korea) (Jung et al., 2026), the NSA-involved pathway begins to emerge but still contributes only marginally to the overall flux. When [NSA] further increases to 10^6-10^7 molecules·cm^{-3}, as in the North China Plain (Nair and Yu, 2020), the NSA-involved pathway rapidly becomes dominant, with its contribution approaching unity, indicating that NSA can substantially enhance nucleation in the NSA-SA-A system. In contrast, at [NSA] = 10^6 molecules·cm^{-3}, *T* exerts a relatively minor influence on pathway partitioning (Fig. 6(c)). Over the *T* range of 258.15-298.15 K, a slight increase in T marginally enhances the contribution of the non-NSA pathway; however, the NSA-involved pathway remains dominant throughout, consistently accounting for more than 80% of the total flux. These results further confirm that NSA plays a decisive role in steering the cluster growth mechanism under atmospherically relevant conditions.

As shown in Fig. 6(d), the contribution of NSA to SA-A aerosol nucleation increases markedly with decreasing [SA]. Under low-SA conditions (10^4 molecules·cm^{-3}), such as those observed in Hyytiälä, the NSA-involved pathway dominates cluster formation, contributing approximately 98% of the total nucleation flux. As [SA] increases to 10^6 molecules·cm^{-3} (e.g., the western coast of Ireland), the contribution of the SA-A-NSA pathway decreases slightly to 95%. However, at higher SA levels (10^7 molecules·cm^{-3}), the NSA-involved pathway is strongly suppressed, accounting for only 3% of the total flux, indicating that low [SA] are more favorable for SA-A-NSA nucleation.

In addition, the contribution of the SA-A-NSA pathway is negatively correlated with [A], as illustrated in Fig. 6(e). In regions with low [A] (10^8 molecules·cm^{-3}), such as Baffin Bay and the eastern Canadian Arctic Archipelago (40-870 pptv) (Wentworth et al., 2016), the NSA-involved pathway contributes about 95%, while the binary SA-A nucleation is nearly negligible. As [A] increases to an intermediate level, typical of Canada (0.8-2.6 ppbv) and America (1.6-4.9 ppbv) (Yao and Zhang, 2016), the contribution of the NSA-involved pathway decreases slightly from 95% to 92%. At even higher [A] (10^{11} molecules·cm^{-3}), such as those observed in Midwest US and the

https://doi.org/10.5194/egusphere-2026-3682
Preprint. Discussion started: 12 August 2026

North China Plain (20-74 ppbv) (Nair and Yu, 2020), its contribution is further reduced to 88%, although it remains the dominant nucleation route. So, the results demonstrate that the contribution of the NSA-involved pathway is significantly enhanced with increasing [NSA] and *T*, and decreasing [SA] and [A]. These results suggest that NSA can act as an important promoter of atmospheric NPF in the SA-A system. In particular, the SA-A-NSA pathway is favorable conditions of relatively high *T* and elevated NSA emissions, particularly in regions with high SO_3 and nitric acid concentrations, such as Beijing and Qingdao.

3.2.4 Competitive effects of NSA and SA on nucleation rates under varying concentration ratios

To evaluate the competitive interaction between NSA and SA, an additional set of ACDC simulations was performed by systematically varying the concentration ratio ([NSA]/[SA]) and the total concentration ([SA] + [NSA]). The nucleation rate, denoted as $J_{NSA/SA}$, was examined over total acid concentrations from 10^4 to 10^8 molecules·cm^{-3}, with [NSA]/[SA] ratios of 1:99, 1:9, 1:1, 9:1, and 99:1. Fig. 7 shows that, at a total acid concentration of 10^4 molecules·cm^{-3}, $J_{NSA/NA}$ remains nearly unchanged at low NSA substitution levels (1% and 10%). However, at 50% substitution ([NSA]/[SA] = 1:1), $J_{NSA/NA}$ increases by approximately one order of magnitude relative to the pure SA system. When substitution reaches 99% ([NSA]/[SA] = 99:1), $J_{NSA/NA}$ attains a maximum value of 1.41×10^{-15} cm^{-3}·s^{-1}. Moreover, $J_{NSA/NA}$ increases by about 15 orders of magnitude as the total acid concentration rises from 10^4 to 10^8 molecules·cm^{-3}. A similar trend is observed under different ammonia concentrations (Fig. S12), with $J_{NSA/NA}$ consistently peaking at 99% NSA substitution. Under this condition, the *J* is enhanced by nearly two orders of magnitude relative to the pure SA system, suggesting that NSA may serve as a more effective nucleation stabilizer than SA.

3.3 The comparison of enhancement effect between NSA and NA

To compare the respective contributions of NSA and NA to SA-A nucleation, we analyzed the ΔG and total evaporation rates $\sum\gamma$ of the $(SA)_x(A)_3(NSA)_y$ and $(SA)_x(A)_3(NA)_y$ ($y = 0$ - 3, $x + y = 3$) clusters at 278.15 K, as depicted in Fig. 8(a). The global minimum structure of the SA-A system, $(SA)_3{\cdot}(A)_3$, was selected as the reference. The ΔG values of all clusters show clear composition-dependent trends. Specifically, the ΔG of the $(SA)_x(A)_3(NSA)_y$ clusters deviate only slightly from the reference. Notably, $(SA)_1{\cdot}(A)_3{\cdot}(NSA)_2$ and $(A)_3{\cdot}(NSA)_3$ exhibit even more negative ΔG values.

https://doi.org/10.5194/egusphere-2026-3682
Preprint. Discussion started: 12 August 2026

With the incorporation of 1 to 3 NSA units, the ΔG difference relative to the reference fluctuates between 5.51 and -2.71 kcal·mol^{-1}. In contrast, all the $(SA)_x(A)_3(NA)_y$ clusters display ΔG values higher than the reference, with a wider variation range. Importantly, ΔG values for NSA-containing clusters are systematically lower than those of their NA-containing counterparts, indicating that NSA enhances cluster stability more effectively than NA.

A closely related trend is observed in the evaporation rates. The total evaporation rates of $(SA)_x(A)_3(NSA)_y$ clusters remain consistently below those of corresponding $(SA)_x(A)_3(NA)_y$ clusters, further confirming the superior stabilizing role of NSA. Within the $(SA)_x(A)_3(NSA)_y$ series, the evaporation rate decreases significantly, spanning approximately seven orders of magnitude, as more NSA molecules are incorporated. In particular, the $(A)_3{\cdot}(NSA)_3$ cluster exhibits a lower evaporation rate than the reference $(SA)_3{\cdot}(A)_3$ cluster. Conversely, evaporation rates of $(SA)_x(A)_3(NA)_y$ tends to increase with the addition of NA molecules. Overall, the SA-A-NSA system exhibits both more negative ΔG and reduced evaporation rates compared to the SA-A-NA system, highlighting its thermodynamic advantage in nucleation, which stems from the stronger binding capacity of NSA toward the SA-A system relative to NA.

The enhancement factors (R) of NA and NSA in SA-A nucleation are compared quantitatively in Fig. 8(b). Over the studied concentration range, NSA induces an enhancement that is orders of magnitude greater than that of NA. As [NSA] increases from 10^3 to 10^7 molecules·cm^{-3}, the enhancement factor $R_{SA\text{-}A\text{-}NSA}$ rises dramatically from ~ 10^2 to over 10^{12}, reflecting an extremely strong promotion of cluster formation. In contrast, the enhancement factor for NA ($R_{SA\text{-}A\text{-}NA}$) remains close to unity and shows negligible variation with increasing NA concentration. Although atmospheric NSA concentrations are typically about five orders of magnitude lower than those of NA, NSA exhibits substantially higher enhancement potential in SA-A-based nucleation. These results clearly demonstrate that NSA is far more effective than NA in enhancing SA-A nucleation, consistent with its superior capability to form intermolecular hydrogen bonds and electrostatic capabilities.

4 Summary and conclusions

In this work, the gas-phase mechanism of NSA formation from the reaction of SO_3 with NA was elucidated using quantum chemical calculations. The role of NSA in SA-A aerosol nucleation,

https://doi.org/10.5194/egusphere-2026-3682
Preprint. Discussion started: 12 August 2026

as well as its nucleation capability relative to the precursor NA was examined through global minimum-energy configuration searches combined with ACDC kinetic simulations.

Quantum chemical calculations indicate that the gas-phase NSA formation from the SO_3 + HNO_3 reaction proceeds with a low energy barrier of 3.61 kcal·mol^{-1}, consistent with previous reports. At low HNO_3 concentrations (< 10^9 molecules·cm^{-3}), the SO_3 + HNO_3 reaction remains more efficient than the SO_3 + HCOOH reaction even under high formic acid levels (> 10^{12} molecules·cm^{-3}; $v_{R1}/v_{R2} \approx 50$). At moderate HNO_3 concentrations (10^{10}-10^{12} molecules·cm^{-3}) and relatively low benzoic acid (10^7-10^8 molecules·cm^{-3}) and NH_3 (10^{10}-10^{11} molecules·cm^{-3}) levels, it effectively competes with both SO_3 + C_6H_5COOH and NH_3-catalyzed SO_3 + NH_3 reactions (v_{R1}/v_{R3} and v_{R1}/v_{R4} up to 10^1-10^3). Under dry conditions (RH = 20%) with HNO_3 exceeding 10^{12} molecules·cm^{-3}, the reaction can even compete with H_2O-catalyzed hydrolysis of SO_3 (v_{R1}/v_{R5} = 1-3).

Geometrical structure analysis reveals that NSA strengthens noncovalent interactions and promotes proton transfer, forming stabilized ion pairs, while thermodynamic analysis demonstrates that NSA incorporation systematically lowers formation free energies, collectively enhancing ternary cluster stability across atmospherically relevant temperatures. ACDC kinetic simulations further demonstrate that NSA plays a significant role in SA-A nucleation, with nucleation rates of SA-A-based clusters reaching approximately 10^{-3} cm^{-3} s^{-1} under heavily polluted urban conditions at 278.15 K such as in Beijing, corresponding to an enhancement of up to five orders of magnitude relative to the binary SA-A clusters. NSA functions as a direct participant in cluster formation pathways, with its contribution increasing markedly at higher concentrations. Compared with nitric acid, NSA exhibits a substantially stronger enhancement effect on nucleation, as reflected by an increase in the ratio R by 10^1-10^{11} orders of magnitude, despite its much lower atmospheric concentration abundance.

This study not only deepens the understanding of the gas-phase formation mechanisms of NSA but also provides new insights into the roles of OSs in aerosol nucleation under heavily polluted urban conditions.

Data availability

All data presented in this study are available upon request from the corresponding author.

Acknowledgments

https://doi.org/10.5194/egusphere-2026-3682
Preprint. Discussion started: 12 August 2026

This work was supported by the National Natural Science Foundation of China (No: 22203052; 22073059), and Yulin Science and Technology Light Talent Program (No: KJZG-2025-K+G-09).

Declaration of competing interest

The authors declare that they have no known competing financial interests or personal relationships that could have appeared to influence the work reported in this paper.

Reference

Almeida, J., Schobesberger, S., Kürten, A., Ortega, I. K., Kupiainen-Määttä, O., Praplan, A. P., Adamov, A., Amorim, A., Bianchi, F., Breitenlechner, M., David, A., Dommen, J., Donahue, N. M., Downard, A., Dunne, E., Duplissy, J., Ehrhart, S., Flagan, R. C., Franchin, A., Guida, R., Hakala, J., Hansel, A., Heinritzi, M., Henschel, H., Jokinen, T., Junninen, H., Kajos, M., Kangasluoma, J., Keskinen, H., Kupc, A., Kurtén, T., Kvashin, A. N., Laaksonen, A., Lehtipalo, K., Leiminger, M., Leppä, J., Loukonen, V., Makhmutov, V., Mathot, S., McGrath, M. J., Nieminen, T., Olenius, T., Onnela, A., Petäjä, T., Riccobono, F., Riipinen, I., Rissanen, M., Rondo, L., Ruuskanen, T., Santos, F. D., Sarnela, N., Schallhart, S., Schnitzhofer, R., Seinfeld, J. H., Simon, M., Sipilä, M., Stozhkov, Y., Stratmann, F., Tomé, A., Tröstl, J., Tsagkogeorgas, G., Vaattovaara, P., Viisanen, Y., Virtanen, A., Vrtala, A., Wagner, P. E., Weingartner, E., Wex, H., Williamson, C., Wimmer, D., Ye, P., Yli-Juuti, T., Carslaw, K. S., Kulmala, M., Curtius, J., Baltensperger, U., Worsnop, D. R., Vehkamäki, H., and Kirkby, J.: Molecular understanding of sulphuric acid-amine particle nucleation in the atmosphere, Nature, 502, 359-363, https://doi.org/10.1038/nature12663, 2013.

Berndt, T., Richters, S., Jokinen, T., Hyttinen, N., Kurtén, T., Otkjær, R. V., Kjaergaard, H. G., Stratmann, F., Herrmann, H., Sipilä, M., Kulmala, M., and Ehn, M.: Hydroxyl radical-induced formation of highly oxidized organic compounds, Nat. Commun., 7, 13677, https://doi.org/10.1038/ncomms13677, 2016.

Brook, R. D., Rajagopalan, S., Pope, C. A., Brook, J. R., Bhatnagar, A., Diez-Roux, A. V., Holguin, F., Hong, Y., Luepker, R. V., Mittleman, M. A., Peters, A., Siscovick, D., Smith, S. C., Whitsel, L., and Kaufman, J. D.: Particulate matter air pollution and cardiovascular disease: an update to the scientific statement from the American Heart Association, 121, 2331-2378, Circulation, https://doi.org/10.1161/CIR.0b013e3181dbece1, 2010.

Casans, A., Casquero-Vera, J. A., Rejano, F., Lyamani, H., Cazorla, A., Zabala, I., Huang, W., Agro, M., Barreto, A., Rodríguez, S., González, Y., Bianchi, F., Petäjä, T., Olmo, F. J., Alados-Arboledas, L., Cariñanos, P., Gysel-Beer, M., and Titos, G.: Determining the impact of new particle formation events on cloud condensation nuclei (CCN) concentrations, Sci. Total Environ., 972, 179094, https://doi.org/10.1016/j.scitotenv.2025.179094, 2025.

Chen, H., Wang, M., Yao, L., Chen, J., and Wang, L.: Uptake of gaseous alkylamides by suspended sulfuric acid particles: formation of ammonium/aminium salts, Environ. Sci. Technol., 51, 11710-11717, https://doi.org/10.1021/acs.est.7b03175, 2017.

Chu, B., Kerminen, V. M., Bianchi, F., Yan, C., Petäjä, T., and Kulmala, M.: Atmospheric new particle formation in China, Atmos. Chem. Phys., 19, 115-138, https://doi.org/10.5194/acp-19-115-2019, 2019.

Dam, M., Thomas, A. E., and Smith, J. N.: Formation of highly oxidized organic compounds and

https://doi.org/10.5194/egusphere-2026-3682
Preprint. Discussion started: 12 August 2026

secondary organic aerosol from α-thujene ozonolysis, J. Phys. Chem. A, 127, 6989-6998, https://doi.org/10.1021/acs.jpca.3c02584, 2023.

Duan, J., Wang, Y., Xie, X., Li, M., Tao, J., Wu, Y., Cheng, T., Zhang, R., Liu, Y., Li, X., He, Q., Gao, W., and Wang, J.: Influence of pollutants on activity of aerosol cloud condensation nuclei (CCN) during pollution and post-rain periods in Guangzhou, southern China, Sci. Total Environ., 642, 1008-1019, https://doi.org/10.1016/j.scitotenv.2018.06.053, 2018.

Elm, J., Bilde, M., and Mikkelsen, K. V.: Assessment of density functional theory in predicting structures and free energies of reaction of atmospheric prenucleation clusters, J. Chem. Theory Comput., 8, 2071-2077, https://doi.org/10.1021/ct300192p, 2012.

Elm, J., and Mikkelsen, K. V.: Computational approaches for efficiently modelling of small atmospheric clusters, Chem. Phys. Lett., 615, 26-29, https://doi.org/10.1016/j.cplett.2014.09.060, 2014.

Frisch, M. J., Trucks, G. W., Schlegel, H. B., Scuseria, G. E., Robb, M. A., Cheeseman, J. R., Scalmani, G., Barone, V., Mennucci, B., Petersson, G. A., Nakatsuji, H., Caricato, M., Li, X., Hratchian, H. P., Izmaylov, A. F., Bloino, J., Zheng, G., Sonnenberg, J. L., Hada, M., Ehara, M., Toyota, K., Fukuda, R., Hasegawa, J., Ishida, M., Nakajima, T., Honda, Y., Kitao, O., Nakai, H., Vreven, T., Montgomery, J. A., Jr., Peralta, J. E., Ogliaro, F., Bearpark, M., Heyd, J. J., Brothers, E., Kudin, K. N., Staroverov, V. N., Kobayashi, R., Normand, J., Raghavachari, K., Rendell, A., Burant, J. C., Iyengar, S. S., Tomasi, J., Cossi, M., Rega, N., Millam, J. M., Klene, M., Knox, J. E., Cross, J. B., Bakken, V., Adamo, C., Jaramillo, J., Gomperts, R., Stratmann, R. E., Yazyev, O., Austin, A. J., Cammi, R., Pomelli, C., Ochterski, J. W., Martin, R. L., Morokuma, K., Zakrzewski, V. G., Voth, G. A., Salvador, P., Dannenberg, J. J., Dapprich, S., Daniels, A. D., Farkas, Ö., Foresman, J. B., Ortiz, J. V., Cioslowski, J., and Fox, D. J: Gaussian09 Revision D. 01, Gaussian Inc. Wallingford CT, Gaussian Inc. Wallingford CT, http://www. gaussian. com, 2009.

Haywood, J., and Boucher, O.: Estimates of the direct and indirect radiative forcing due to tropospheric aerosols: A review, Rev. Geophys., 38, 513-543, https://doi.org/10.1029/1999RG000078, 2000.

Hazra, M. K., and Sinha, A.: Formic acid catalyzed hydrolysis of SO_3 in the gas phase: a barrierless mechanism for sulfuric acid production of potential atmospheric importance, J. Am. Chem. Soc., 133, 17444-17453, https://doi.org/10.1021/ja207393v, 2011.

Holtomo, O., Mbigah, M. D., Nsangou, M., and Motapon, O.: Insight of UV-vis spectra and atmospheric implication for the reaction of ˙OH radical towards glyphosate herbicide and its hydrates, RSC Adv., 11, 16404-16418, https://doi.org/10.1039/D1RA01591E, 2021.

Hunt, S. W., Higgins, K. J., Craddock, M. B., Brauer, C. S., and Leopold, K. R.: Influence of a polar near-neighbor on incipient proton transfer in a strongly hydrogen bonded complex, J. Am. Chem. Soc., 125, 13850-13860, https://doi.org/10.1021/ja030435x, 2003.

Jung, D., Song, J., Kim, K., Kang, S., Kim, Y., Hong, S.-C., Lee, J.-B., Seo, S.-J., Lee, K., Park, J.-S., Song, M., Choi, N. R., and Lee, T.: Spatial and Seasonal Variation of Nitric Acid (HNO_3) and Understanding the Formation of NH_4NO_3 in the HNO_3-NH_3 system in Korea, Aerosol and Air Quality Research, 26, 19, https://doi.org/10.1007/s44408-025-00090-2, 2026.

Kirkby, J., Curtius, J., Almeida, J., Dunne, E., Duplissy, J., Ehrhart, S., Franchin, A., Gagné, S., Ickes, L., Kürten, A., Kupc, A., Metzger, A., Riccobono, F., Rondo, L., Schobesberger, S., Tsagkogeorgas, G., Wimmer, D., Amorim, A., Bianchi, F., Breitenlechner, M., David, A., Dommen, J., Downard, A., Ehn, M., Flagan, R. C., Haider, S., Hansel, A., Hauser, D., Jud, W., Junninen, H., Kreissl, F., Kvashin, A., Laaksonen, A., Lehtipalo, K., Lima, J., Lovejoy, E. R., Makhmutov, V., Mathot, S., Mikkilä, J., Minginette, P., Mogo, S., Nieminen, T., Onnela, A., Pereira, P., Petäjä, T., Schnitzhofer, R., Seinfeld,

https://doi.org/10.5194/egusphere-2026-3682
Preprint. Discussion started: 12 August 2026

J. H., Sipilä, M., Stozhkov, Y., Stratmann, F., Tomé, A., Vanhanen, J., Viisanen, Y., Vrtala, A., Wagner, P. E., Walther, H., Weingartner, E., Wex, H., Winkler, P. M., Carslaw, K. S., Worsnop, D. R., Baltensperger, U., and Kulmala, M.: Role of sulphuric acid, ammonia and galactic cosmic rays in atmospheric aerosol nucleation, Nature, 476, 429-433, https://doi.org/10.1038/nature10343, 2011.

Kuang, C., McMurry, P. H., McCormick, A. V., and Eisele, F.: Dependence of nucleation rates on sulfuric acid vapor concentration in diverse atmospheric locations, J Geophys Res-Atomos, 113, https://doi.org/10.1029/2007JD009253, 2008.

Kulmala, M., Kontkanen, J., Junninen, H., Lehtipalo, K., Manninen, H. E., Nieminen, T., Petäjä, T., Sipilä, M., Schobesberger, S., Rantala, P., Franchin, A., Jokinen, T., Järvinen, E., Äijälä, M., Kangasluoma, J., Hakala, J., Aalto, P. P., Paasonen, P., Mikkilä, J., Vanhanen, J., Aalto, J., Hakola, H., Makkonen, U., Ruuskanen, T., Mauldin, R. L., Duplissy, J., Vehkamäki, H., Bäck, J., Kortelainen, A., Riipinen, I., Kurtén, T., Johnston, M. V., Smith, J. N., Ehn, M., Mentel, T. F., Lehtinen, K. E. J., Laaksonen, A., Kerminen, V.-M., and Worsnop, D. R.: Direct observations of atmospheric aerosol nucleation, Science, 339, 943-946, https://doi.org/10.1126/science.1227385, 2013.

Kürten, A., Jokinen, T., Simon, M., Sipilä, M., Sarnela, N., Junninen, H., Adamov, A., Almeida, J., Amorim, A., and Bianchi, F.: Neutral molecular cluster formation of sulfuric acid-dimethylamine observed in real time under atmospheric conditions, Proc. Natl. Acad. Sci. U.S.A., 111, 15019-15024, https://doi.org/10.1073/pnas.1404853111, 2014.

Lee, S.-H., Gordon, H., Yu, H., Lehtipalo, K., Haley, R., Li, Y., and Zhang, R.: New particle formation in the atmosphere: from molecular clusters to global climate, J GEOPHYS RES-ATMOS, 124, 7098-7146, https://doi.org/10.1029/2018JD029356, 2019.

Li, H., Zhong, J., Vehkamäki, H., Kurtén, T., Wang, W., Ge, M., Zhang, S., Li, Z., Zhang, X., Francisco, J. S., and Zeng, X. C.: Self-catalytic reaction of SO_3 and NH_3 to produce sulfamic acid and its implication to atmospheric particle formation, J. Am. Chem. Soc., 140, 11020-11028, https://doi.org/10.1021/jacs.8b04928, 2018.

Li, J., Ning, A., Liu, L., and Zhang, X.: Atmospheric bases-enhanced iodic acid nucleation: altitude-dependent characteristics and molecular mechanisms, Environ. Sci. Technol., 58, 16962-16973, https://doi.org/10.1021/acs.est.4c06053, 2024a.

Li, J., Wu, N., Chu, B., Ning, A., and Zhang, X.: Molecular-level study on the role of methanesulfonic acid in iodine oxoacid nucleation, Atmos. Chem. Phys., 24, 3989-4000, https://doi.org/10.1021/acs.est.4c06053, 2024b.

Liu, J., Liu, L., Rong, H., and Zhang, X.: The potential mechanism of atmospheric new particle formation involving amino acids with multiple functional groups, Phys. Chem. Chem. Phys., 23, 10184-10195, https://doi.org/10.1039/D0CP06472F, 2021.

Liu, L., Li, H., Zhang, H., Zhong, J., Bai, Y., Ge, M., Li, Z., Chen, Y., and Zhang, X.: The role of nitric acid in atmospheric new particle formation, Phys. Chem. Chem. Phys., 20, 17406-17414, https://doi.org/10.1039/C8CP02719F, 2018.

Liu, L., Zhong, J., Vehkamäki, H., Kurtén, T., Du, L., Zhang, X., Francisco, J. S., and Zeng, X. C.: Unexpected quenching effect on new particle formation from the atmospheric reaction of methanol with SO_3, Proc. Natl. Acad. Sci. U.S.A., 116, 24966-24971, https://doi.org/10.1073/pnas.1915459116, 2019.

Long, B., Xia, Y., Bao, J. L., Carmona-García, J., Gómez Martín, J. C., Plane, J. M. C., Saiz-Lopez, A., Roca-Sanjuán, D., and Francisco, J. S.: Reaction of SO_3 with $HONO_2$ and implications for sulfur partitioning in the atmosphere, J. Am. Chem. Soc., 144, 9172-9177,

https://doi.org/10.5194/egusphere-2026-3682
Preprint. Discussion started: 12 August 2026

https://doi.org/10.1021/jacs.2c03499, 2022.

Mäkelä, J. M., Aalto, P., Jokinen, V., Pohja, T., Nissinen, A., Palmroth, S., Markkanen, T., Seitsonen, K., Lihavainen, H., and Kulmala, M.: Observations of ultrafine aerosol particle formation and growth in boreal forest, Geophys. Res. Lett., 24, 1219-1222, https://doi.org/10.1029/97GL00920, 1997.

Mayntz, S. P., Warncke, S., Ladefoged, L. G., Mohamed, R. A., Mejldal, A., Lindholt, J. S., Diederichsen, A. C. P., Frohn, L. M., Brandt, J., Ketzel, M., Khan, J., and Lambrechtsen, J.: The role of long-term fine particulate matter peaks in cardiovascular risk: an AIRCARD substudy, J Cardiol, 86, 387-394, https://doi.org/10.1016/j.jjcc.2025.04.012, 2025.

McNeill, V. F.: Atmospheric aerosols: clouds, chemistry, and climate, Annu. Rev. Chem. Biomol. Eng., 8, 427-444, https://doi.org/10.1146/annurev-chembioeng-060816-101538, 2017.

Myllys, N., Kubečka, J., Besel, V., Alfaouri, D., Olenius, T., Smith, J. N., and Passananti, M.: Role of base strength, cluster structure and charge in sulfuric-acid-driven particle formation, Atmos. Chem. Phys., 19, 9753-9768, https://doi.org/10.5194/acp-19-9753-2019, 2019.

Nair, A. A., and Yu, F.: Quantification of atmospheric ammonia concentrations: A review of its measurement and modeling, Atmosphere, 11, 1092, https://doi.org/10.3390/atmos11101092, 2020.

Neese, F.: Software update: the ORCA program system, version 4.0, Wires. Comput. Mol. Sci., 8, https://doi.org/10.1002/wcms.1327, 2018.

Partanen, L., Vehkamäki, H., Hansen, K., Elm, J., Henschel, H., Kurtén, T., Halonen, R., and Zapadinsky, E.: Effect of conformers on free energies of atmospheric complexes, J. Phys. Chem. A, 120, 8613-8624, https://doi.org/10.1021/acs.jpca.6b04452, 2016.

Pope, C. A., Cohen, A. J., and Burnett, R. T.: Cardiovascular disease and fine particulate matter: lessons and limitations of an integrated exposure-response approach, Circ. Res., 122, 1645-1647, https://doi.org/10.1161/CIRCRESAHA.118.312956, 2018.

Pöschl, U.: Atmospheric aerosols: composition, transformation, climate and health effects, ANGEW CHEM INT EDIT, 44, 7520-7540, https://doi.org/10.1002/anie.200501122, 2005.

Qi, J. M., Sun, H. T., Huang, Z. J., Shi, Z. P., Duan, L. B.: Migration characteristics of SO_3 and condensable particulate matters in ultra-low emission coal-fired power plants, Therm. Power Gener., 50, 72-77, https://doi.org/10.19666/j.rlfd.202007225, 2021.

Rong, H., Liu, J., Zhang, Y., Du, L., Zhang, X., and Li, Z.: Nucleation mechanisms of iodic acid in clean and polluted coastal regions, Chemosphere, 253, 126743, https://doi.org/10.1016/j.chemosphere.2020.126743, 2020.

Shampine, L. F., and Reichelt, M. W.: The MATLAB ODE Suite, SIAM J. Sci. Comput., 18, 1-22, https://doi.org/10.1137/S1064827594276424, 1997.

Silva, K. M. R. d., Herdies, D. L., Kubota, P. Y., Bresciani, C., and Figueroa, S. N.: Impact of aerosols on cloud microphysical processes: a theoretical review, Geosciences, 15, 312, https://doi.org/10.3390/geosciences15080312, 2025.

Sipilä, M., Berndt, T., Petäjä, T., Brus, D., Vanhanen, J., Stratmann, F., Patokoski, J., Mauldin III, R. L., Hyvärinen, A. P., and Lihavainen, H.: The role of sulfuric acid in atmospheric nucleation, Science, 327, 1243-1246, https://www.science.org/doi/10.1126/science.1180315, 2010.

Smith, C. J., Huff, A. K., Ward, R. M., and Leopold, K. R.: Carboxylic sulfuric anhydrides, J. Phys. Chem. A, 124, 601-612, https://doi.org/10.1021/acs.jpca.9b09310, 2020.

Stewart, J. J.: Optimization of parameters for semiempirical methods VI: more modifications to the NDDO approximations and re-optimization of parameters, J. Mol. Model., 19, 1-32, https://doi.org/10.1007/s00894-012-1667-x, 2013.

https://doi.org/10.5194/egusphere-2026-3682
Preprint. Discussion started: 12 August 2026

Sun, Y., Luo, H., Li, Y., Zhou, W., Xu, W., Fu, P., and Zhao, D.: Atmospheric organic aerosols: online molecular characterization and environmental impacts, npj Clim Atmos Sci , 8, 305, https://doi.org/10.1038/s41612-025-01199-2, 2025.

Chen, Z. M., Liu, H. X., Cui, Y., Guo, G. F., Meng, Y. C., Liu, M. L., He, H. T., Fang, X. W.: Study on generation, hazard, testing and emission characteristics of SO_3 in flue gas of coal-fired power plants, Power Gener. Technol., 40, 564-569, https://doi.org/10.12096/j.2096-4528.pgt.19096, 2019.

Wang, Q., Xie, H., Chen, Y., and Liu, C.: Effects of temperature and pressure on the nucleation and growth of silver clusters from supersaturated vapor: A molecular dynamics analysis, Int. J. Mod. Phys. B, 31, 1750057, https://doi.org/10.1142/S0217979217500576, 2017.

Wang, R., Li, R. R., Chen, S. S., Mu, R. X., Zhang, C. M., Ma, X. H., Khan, M., and Zhang, T. L,: Enhancing SO_3 hydrolysis and nucleation: the role of formic sulfuric anhydride, Atmos. Chem. Phys., 25, 5695-5709, https://doi.org/10.5194/acp-25-5695-2025, 2025.

Wang, Z. Q., Liu, Y. R., Wang, C. Y., Jiang, S., Feng, Y. J., Huang, T., and Huang, W.: The nucleation mechanism of succinic acid involved sulfuric acid-Dimethylamine in new particle formation, Atmos. Environ., 263, 118683, https://doi.org/10.1016/j.atmosenv.2021.118683, 2021.

Wentworth, G. R., Murphy, J. G., Croft, B., Martin, R. V., Pierce, J. R., Côté, J. S., Courchesne, I., Tremblay, J. É., Gagnon, J., Thomas, J. L., Sharma, S., Toom-Sauntry, D., Chivulescu, A., Levasseur, M., and Abbatt, J. P. D.: Ammonia in the summertime Arctic marine boundary layer: sources, sinks, and implications, Atmos. Chem. Phys., 16, 1937-1953, https://doi.org/10.5194/acp-16-1937-2016, 2016.

Williamson C. J., Kupc A., Axisa D., Bilsback K. R., Bui T., Campuzano-Jost P., Dollner M., Froyd K. D., Hodshire A. L., Jimenez J. L., Kodros J. K., Luo G., Murphy D. M., Nault B. A., Ray E. A., Weinzierl B., Wilson J. C., Yu F., Yu P., Pierce J. R., Brock C. A.: A large source of cloud condensation nuclei from new particle formation in the tropics, Nature, 574, 399-403, https://doi.org/10.1038/s41586-019-1638-9, 2019.

Xu, C. X., Jiang, S., Liu, Y. R., Feng, Y. J., Wang, Z. H., Huang, T., Zhao, Y., Li, J., and Huang, W.: Formation of atmospheric molecular clusters of methanesulfonic acid-diethylamine complex and its atmospheric significance, Atmos. Environ., 226, 117404, https://doi.org/10.1016/j.atmosenv.2020.117404, 2020.

Yang, Y., Liu, L., Wang, H., and Zhang, X.: Molecular-scale mechanism of sequential reaction of oxalic acid with SO_3: potential participator in atmospheric aerosol nucleation, J. Phys. Chem. A, 125, 4200-4208, https://doi.org/10.1021/acs.jpca.1c02113, 2021.

Yao, L., Fan, X., Yan, C., Kurtén, T., Daellenbach, K. R., Li, C., Wang, Y., Guo, Y., Dada, L., Rissanen, M. P., Cai, J., Tham, Y. J., Zha, Q., Zhang, S., Du, W., Yu, M., Zheng, F., Zhou, Y., Kontkanen, J., Chan, T., Shen, J., Kujansuu, J. T., Kangasluoma, J., Jiang, J., Wang, L., Worsnop, D. R., Petäjä, T., Kerminen, V.-M., Liu, Y., Chu, B., He, H., Kulmala, M., and Bianchi, F.: Unprecedented ambient sulfur trioxide (SO_3) detection: possible formation mechanism and atmospheric implications, Environ. Sci. Technol. Lett., 7, 809-818, https://doi.org/10.1021/acs.estlett.0c00615, 2020.

Yao, X., and Zhang, L.: Trends in atmospheric ammonia at urban, rural, and remote sites across North America, Atmos. Chem. Phys., 16, 11465-11475, https://doi.org/10.5194/acp-16-11465-2016, 2016.

Yu, F., Nadykto, A. B., Herb, J., Luo, G., Nazarenko, K. M., and Uvarova, L. A.: H_2SO_4-H_2O-NH_3 ternary ion-mediated nucleation (TIMN): kinetic-based model and comparison with CLOUD measurements, Atmos. Chem. Phys., 18, 17451-17474, https://doi.org/10.5194/acp-18-17451-2018, 2018.

Zbieranowski, A. L., and Aherne, J.: Ambient concentrations of atmospheric ammonia, nitrogen dioxide

https://doi.org/10.5194/egusphere-2026-3682
Preprint. Discussion started: 12 August 2026

and nitric acid across a rural-urban-agricultural transect in southern Ontario, Canada, Atmos. Environ., 62, 481-491, https://doi.org/10.1016/j.atmosenv.2012.08.040, 2012.

Zhang, J., and Dolg, M.: ABCluster: the artificial bee colony algorithm for cluster global optimization, Phys. Chem. Chem. Phys., 17, 24173-24181, https://doi.org/10.1039/C5CP04060D, 2015.

Zhang, J., and Dolg, M.: Global optimization of clusters of rigid molecules using the artificial bee colony algorithm, Phys. Chem. Chem. Phys., 18, 3003-3010, https://doi.org/10.1039/C5CP06313B, 2016.

Zhang, R., Khalizov, A., Wang, L., Hu, M., and Xu, W.: Nucleation and growth of nanoparticles in the atmosphere, Chem. Rev., 112, 1957-2011, https://doi.org/10.1021/cr2001756, 2012.

Zhang, X., Tan, S., Chen, X., and Yin, S.: Computational chemistry of cluster: understanding the mechanism of atmospheric new particle formation at the molecular level, Chemosphere, 308, 136109, https://doi.org/10.1016/j.chemosphere.2022.136109, 2022.

Zhang, X., Lian, Y., Tan, S., and Yin, S.: Organosulfate produced from consumption of SO_3 speeds up sulfuric acid-dimethylamine atmospheric nucleation, Atmos. Chem. Phys., 24, 3593-3612, https://doi.org/10.5194/acp-24-3593-2024, 2024.

Zhao, N., Al-Aly, Z., van Donkelaar, A., Martin, R. V., Assayag, D., Pineau, C. A., and Bernatsky, S.: Fine particulate matter and interstitial lung disease in systemic autoimmune rheumatic diseases, Eur Respir J., 65, https://doi.org/10.1183/13993003.02403-2024, 2025.

Zuo, C., Zhao, X., Wang, H., Ma, X., Zheng, S., Xu, F., and Zhang, Q.: A theoretical study of hydrogen-bonded molecular clusters of sulfuric acid and organic acids with amides, J. Environ. Sci., 100, 328-339, https://doi.org/10.1016/j.jes.2020.07.022, 2021.

https://doi.org/10.5194/egusphere-2026-3682
Preprint. Discussion started: 12 August 2026

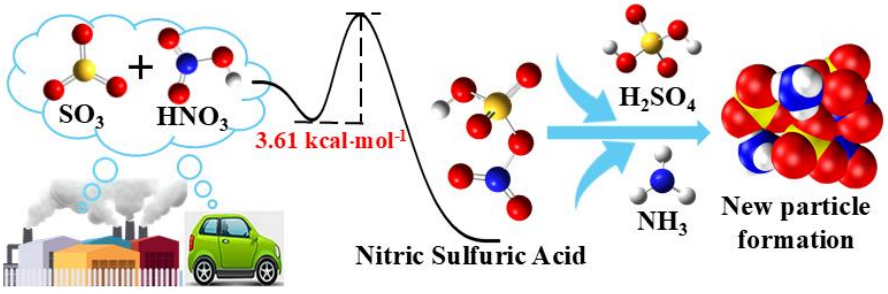

Graphic Abstract

https://doi.org/10.5194/egusphere-2026-3682
Preprint. Discussion started: 12 August 2026

Figure Caption

Fig. 1 Interaction Region Indicator (IRI) analysis of representative structures along the reaction pathway. Shown are sign (λ_2)ρ-mapped isosurfaces at IRI = 1.0, where sign (λ_2) is the sign of the second largest eigenvalue (λ_2) of the electron density Hessian matrix, and ρ represents the electron density (higher ρ values indicate stronger bonding interactions). Energies are relative values obtained at the CCSD(T)-F12/cc-pVDZ-F12//M06-2X/6-311++G(2*df*,2*pd*) level of theory. (a), (c) and (f) represent reactant complex ($SO_3\cdots HNO_3$), transition state (TS) and product (NSA), respectively, while (b), (d), and (e) represent unstable points along the IRC pathway.

Fig. 2 Rate ratios of v_{R1}/v_{R2} (a), v_{R1}/v_{R3} (b), v_{R1}/v_{R4} (c) and v_{R1}/v_{R5} (d) at 298 K.

Fig. 3 The most stable configurations of ternary clusters of $(NSA)_x(SA)_y(A)_z$ ($z \leq x + y \leq 3$) clusters identified at the M06-2X/6-311++G(2*df*,2*pd*) level. The white, red, yellow, and blue spheres represent the H, O, S, and N atoms, respectively.

Fig. 4 Gibbs formation free energies (ΔG, kcal·mol^{-1}) of the growing clusters in the SA-A-NS (A = acid, B = base) at 278.15 K at the DLPNO-CCSD(T)/aug-cc-pVTZ//M06-2X/6-311++G(2*df*,2*pd*) level of theory.

Fig. 5 (a) Cluster formation rates J (cm^{-3} s^{-1}) against the of NSA monomer concentration under different temperatures (258.15, 268.15, 278.15, 288.15, and 298.15 K), where [SA] = 10^6 molecules·cm^{-3} and [A] = 10^9 molecules·cm^{-3}; (b) Cluster formation rates J (cm^{-3} s^{-1}) as a function of sulfuric acid concentration [SA] (10^4-10^8 molecules·cm^{-3}) and base concentration [A] (10^7-10^{11} molecules·cm^{-3}) at T = 278.15K, where [NSA] = 10^6 molecules·cm^{-3}.

Fig. 6 Nucleation mechanism of the SA-A-NSA system. (a) cluster formation pathway at T = 278.15 K, [SA] = 10^6 molecules·cm^{-3}, [A] = 10^9 molecules·cm^{-3} and [NSA] = 10^6 molecules·cm^{-3}; (b) contribution of pathway to flux out and (c) enhancement of cluster formation rate J (cm^{-3} s^{-1}). Simulations in (b and c) were conducted at T = 278.15 K, [SA] = 10^6 molecules·cm^{-3}, [A] = 10^9 molecules·cm^{-3} and [NSA] = 10^3-10^7 molecules·cm^{-3}.

Fig. 7 The cluster formation rate as a function of the ratio [NSA]/[SA] at a simulated temperature of 278.15 K and A molecular concentrations of 10^9 molecules·cm^{-3}. The concentrations of NSA and SA are collectively maintained constant (10^4-10^9 molecules·cm^{-3}).

Fig. 8 (a) Gibbs free energies ΔG (kcal·mol^{-1})and total evaporation rates $\sum\gamma$ (s^{-1}) for

https://doi.org/10.5194/egusphere-2026-3682
Preprint. Discussion started: 12 August 2026

$(SA)_x(A)_y(NSA)_z$; and $(SA)_x(A)_y(NA)_z$ (x = 0-3, $x + y = 3$) clusters calculated at the DLPNO-CCSD(T)/aug-cc-pVTZ//M06-2X/6311++G(2*df*,2*pd*) level of theory and 278.15 K, (b) Cluster formation rate (J) for NSA as a function of monomer concentrations [NSA] and [NA])) at 238.15 K, with [SA] fixed at 10^4 molecules·cm^{-3} and [A] at 10^7 molecules·cm^{-3}.

https://doi.org/10.5194/egusphere-2026-3682
Preprint. Discussion started: 12 August 2026

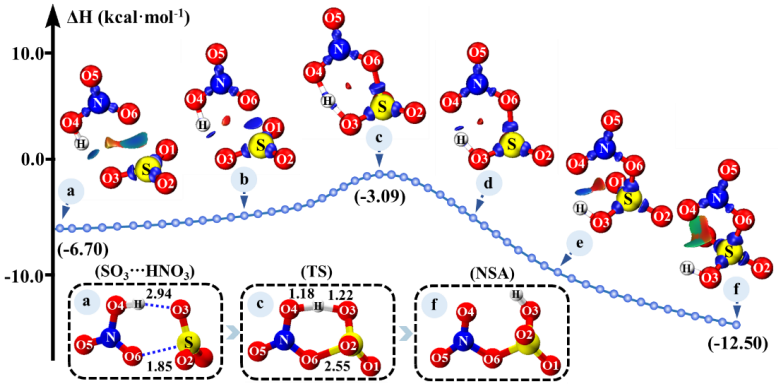

Fig. 1

https://doi.org/10.5194/egusphere-2026-3682
Preprint. Discussion started: 12 August 2026

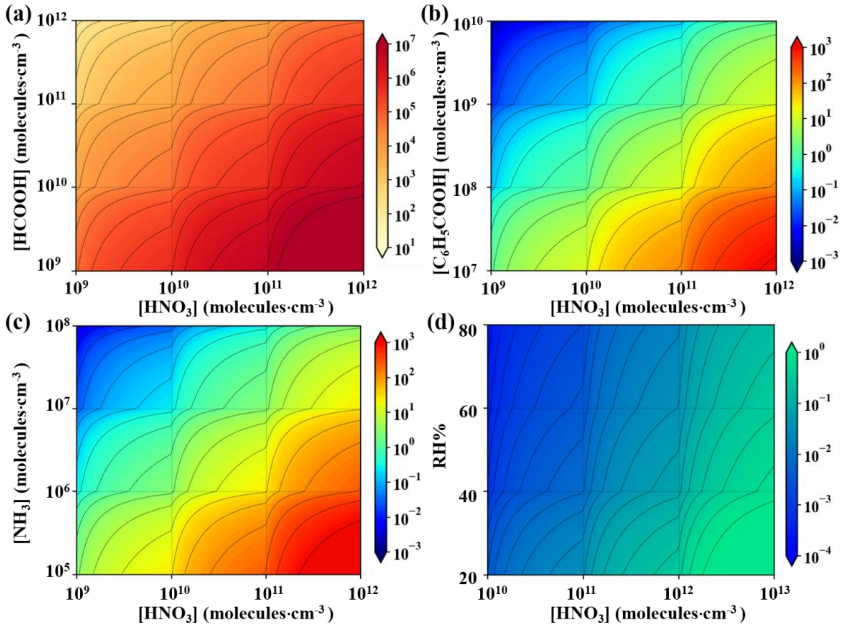

Fig. 2

https://doi.org/10.5194/egusphere-2026-3682
Preprint. Discussion started: 12 August 2026

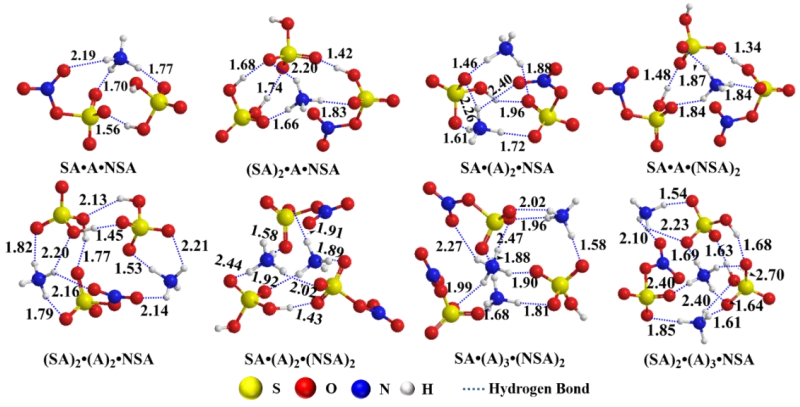

667

668 **Fig. 3**

669

670

https://doi.org/10.5194/egusphere-2026-3682
Preprint. Discussion started: 12 August 2026

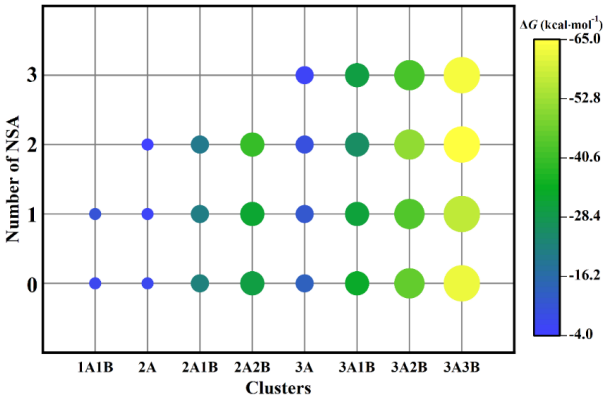

671
672 **Fig. 4**
673

https://doi.org/10.5194/egusphere-2026-3682
Preprint. Discussion started: 12 August 2026

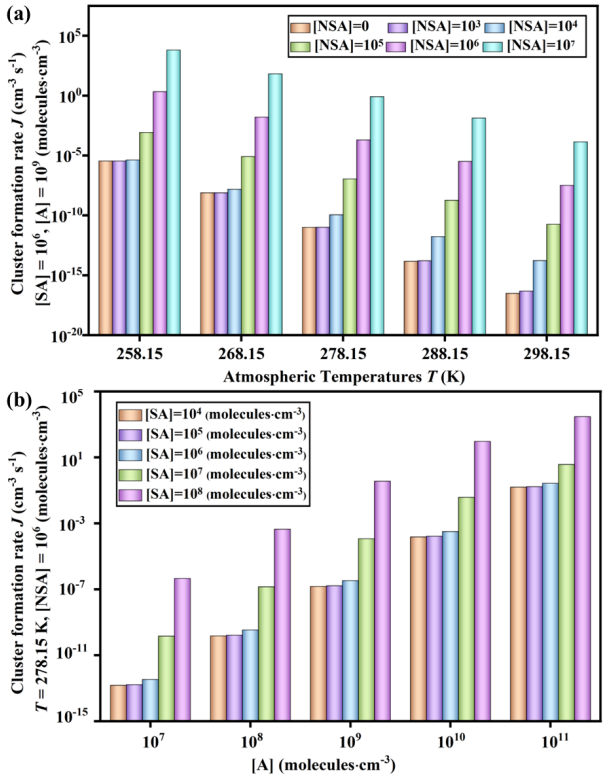

Fig. 5

https://doi.org/10.5194/egusphere-2026-3682
Preprint. Discussion started: 12 August 2026

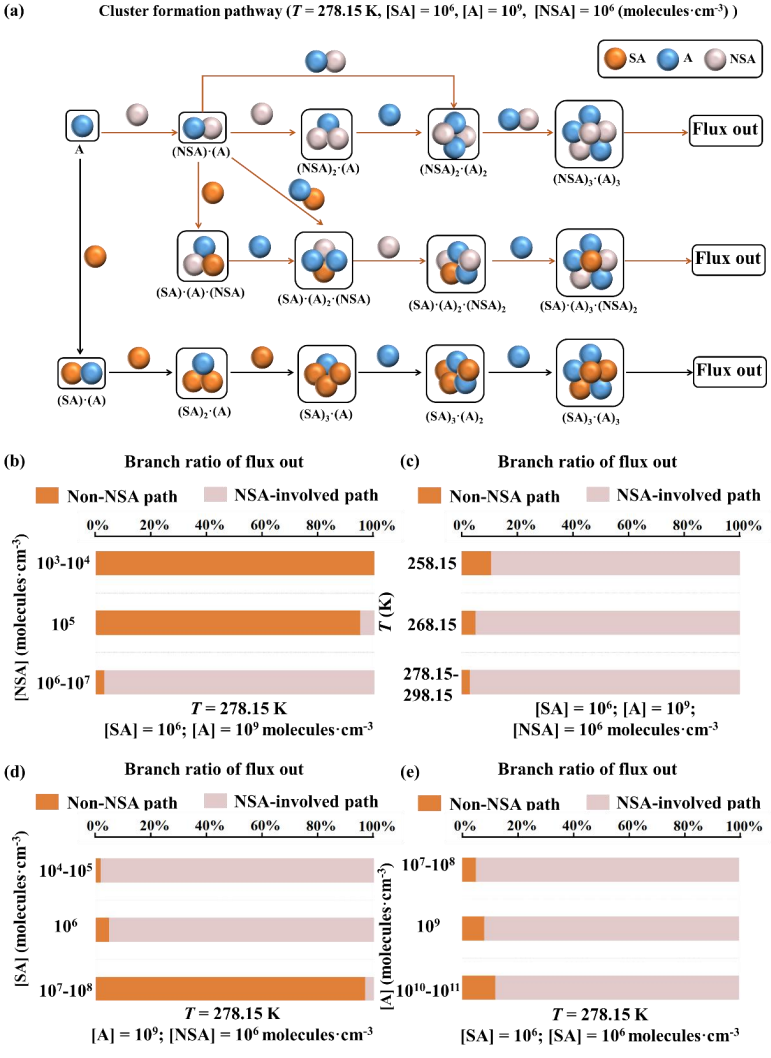

Fig. 6

https://doi.org/10.5194/egusphere-2026-3682
Preprint. Discussion started: 12 August 2026

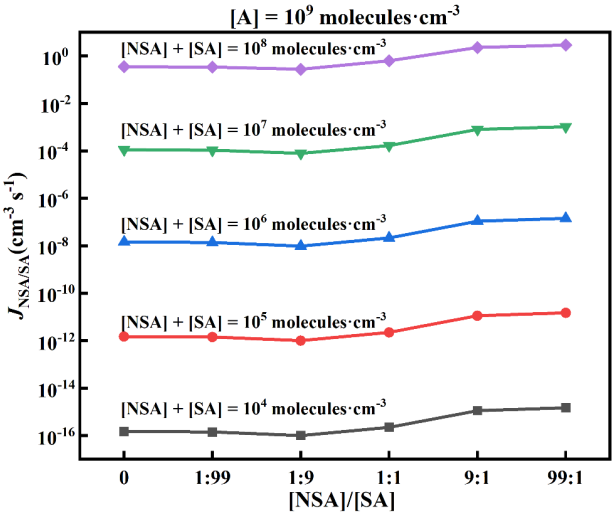

680
681 **Fig. 7**
682
683

https://doi.org/10.5194/egusphere-2026-3682
Preprint. Discussion started: 12 August 2026

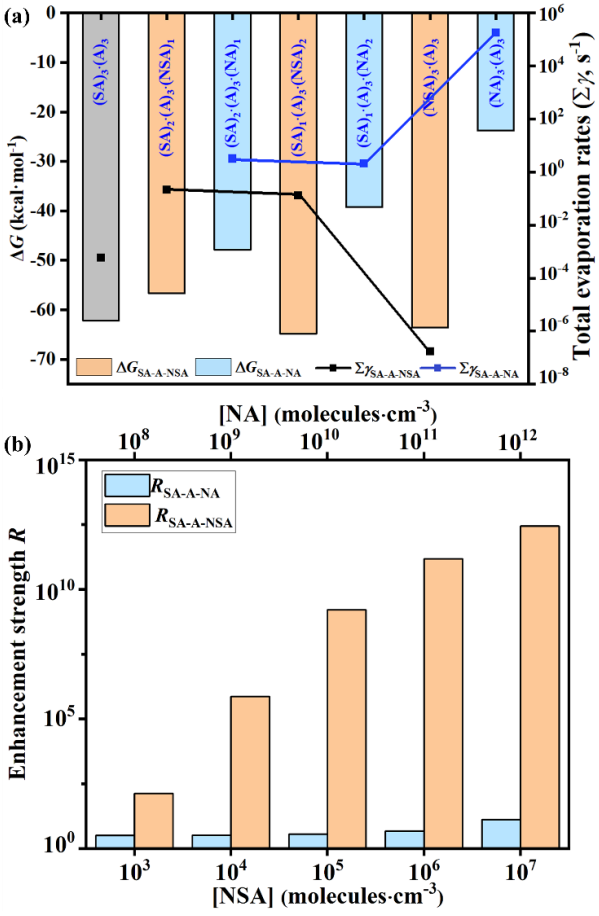

684
685 **Fig. 8**
686

https://doi.org/10.5194/egusphere-2026-3682
Preprint. Discussion started: 12 August 2026

Table 1 Proton-transfer parameter (ρ_{PT}/Å) of the nitrogen-hydrogen bond in the clusters. The total number of proton transfers (n) and the proton donor and acceptor are also listed.

Cluster	r_{OH}	$r_{N\cdots H}$	ρ_{PT}	Proton donor	Proton acceptor	n
SA·A·NSA	1.699	1.048	0.697	NSA	A	1
$(SA)_2$·A·NSA	2.571	1.032	1.585	SA	A	1
SA·$(A)_2$·NSA	1.721	1.040	0.727	NSA	A	2
	1.464	1.101	0.409	SA	A	
SA·A·$(NSA)_2$	1.869	1.034	0.881	SA	A	1
$(SA)_2$·$(A)_2$·NSA	1.785	1.039	0.792	NSA	A	2
	1.530	1.082	0.494	SA	A	
SA·$(A)_2$·$(NSA)_2$	1.578	1.061	0.563	NSA	A	2
	1.923	1.031	0.938	SA	A	
SA·$(A)_3$·$(NSA)_2$	1.683	1.043	0.686	NSA	A	3
	1.903	1.031	0.918	NSA	A	
	1.583	1.066	0.563	SA	A	
$(SA)_2$·$(A)_3$·NSA	1.848	1.034	0.860	NSA	A	3
	2.229	1.023	1.252	SA	A	
	2.704	1.015	1.735	SA	A	